ACS OMEGA

Article

Cite This: ACS Omega 2018, 3, 13828−13836

http://pubs.acs.org/journal/acsodf

Efficient Visible-Light Photocatalysis of 2D-MXene Nanohybrids with Gd^{3+}- and Sn^{4+}-Codoped Bismuth Ferrite

Ayesha Tariq,[†] S. Irfan Ali,[‡,§] Deji Akinwande,[∥] and Syed Rizwan*[,†]

[†]Department of Physics, School of Natural Sciences (SNS), National University of Sciences and Technology (NUST), Islamabad 44000, Pakistan

[‡]Shenzhen Key Laboratory of Advanced Thin Films and Applications, College of Physics and Energy and [§]Key Laboratory of Optoelectronic Devices and Systems of Ministry of Education and Guangdong Province, College of Optoelectronic Engineering, Shenzhen University, Shenzhen 518060, China

[∥]Microelectronics Research Center, The University of Texas at Austin, Austin, Texas 78758, United States

ABSTRACT: Nowadays, photocatalysis has gained tremendous interest owing to the fact that it can overcome water crisis as well as the environmental issues by utilizing a major source of solar energy. The nanohybrid structures of Gd^{3+}- and Sn^{4+}-doped bismuth ferrite ($Bi_{1-x}Gd_xFe_{1-y}Sn_y$; BGFSO) with two-dimensional (2D) MXene sheets are synthesized by the coprecipitation method. The 2D sheets have a large surface area, incorporation of which into $Bi_{1-x}Gd_xFe_{1-y}Sn_y$ (BGFSO) nanoparticles provides a path for electrons to flow, which results in large recombination time and thus enhances dye degradation. The $Bi_{0.90}Gd_{0.10}Fe_{0.80}Sn_{0.20}O_3$/MXene (BGFO-20Sn/MXene) nanohybrid shows 100% degradation of Congo dye from the catalytic solution in 120 min, which is highly efficient for industrial application.

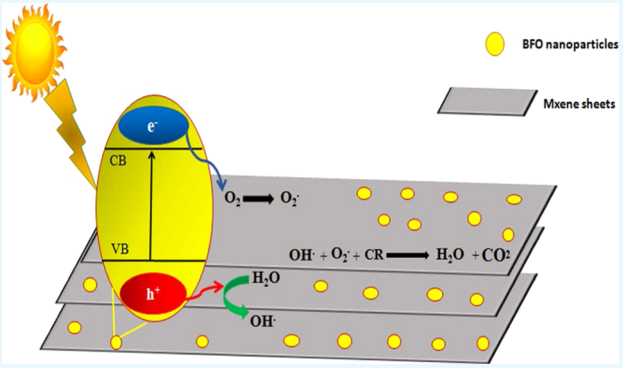

1. INTRODUCTION

Over the last few years, a vast increase in environmental pollution has taken place, which introduces the contaminants into the environment causing instability, harm, or disorder to the ecosystem. Water pollution that occurs due to the industrial wastes containing toxic chemicals affects human life and interrupts photosynthetic activity; decreases soil fertility; affects the production of crops; induces toxicity to aquatic life; and causes hazardous diseases such as skin cancer, skin allergies, etc. These potential risks related to polluted water rivers have been increased vastly by the discharge of innumerable kinds of textile organic dyes into fresh water streams, consequently, producing wastewaters. Due to the increasing demand of potable water, it is necessary to treat polluted water to make it purified and useful for drinking purposes.[1]

Photocatalysis is a low-cost and useful technique to purify water from different organic pollutants with end product in the form of water molecules and carbon dioxide. Congo red (CR) is a benzidine-based azo dye containing an anionic complex structure. The treatment of polluted water containing Congo red dye is difficult due to the complicated anionic structure that opposes its degradation.

Metal oxide-based photocatalysts are helpful in purifying the polluted water by the removal of hazardous compounds like organic dyes (such as Congo red).[2−5] A photocatalyst is a material that undergoes oxidation and reduction reactions on the material surface in the presence of charged particles, i.e., electrons and holes, which further generate the species that help out in dye degradation from a solution.[6]

In the past, the abundantly available semiconductor-based photocatalysts have been used to degrade organic dyes due to the fact that they are easily recyclable. The n-type and p-type semiconductors both act as a photocatalyst.[7] In earlier times, TiO_2 with a band gap of 3.2 eV and ZnO with a band gap of 3.4 eV were used efficiently, but their efficiency was not good due to their wide band gaps.[8−10] Meanwhile, visible-light-active materials got more attention than UV-active materials due to their narrow band gaps (2.1 eV). Recently, $BiFeO_3$ (BFO) was found to be a promising candidate for photocatalysis due to its low band gap (2.2−2.6 eV) and mesoporous structure. The band gap of BFO is further tuned by doping metal ions such as tin (Sn^{4+}), gadolinium (Gd^{3+}), etc. The tuning of band gap increases the charge generation as well as its separation because of the formation of intermediate energy levels between the valence band (VB) and the conduction band (CB).[11] The doping of various metal ions into BFO nanoparticles also decreases the crystallite size because of the decrease in the nucleation rate due to the distortions induced in the crystal structure, thus enhancing the surface area. The enhanced

Received: August 8, 2018
Accepted: October 10, 2018
Published: October 22, 2018

DOI: 10.1021/acsomega.8b01951
ACS Omega 2018, 3, 13828−13836

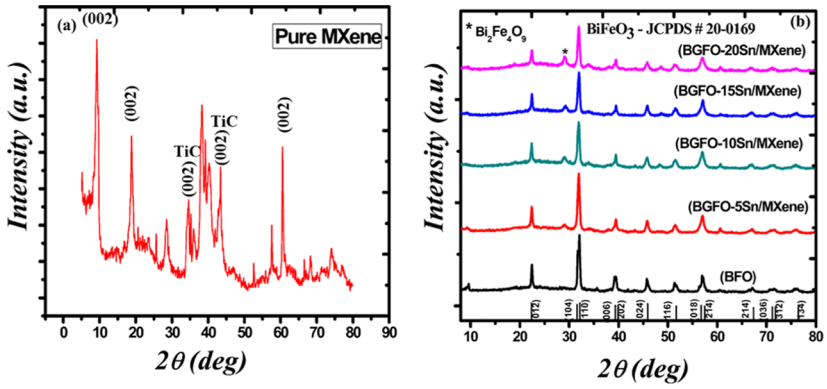

Figure 1. XRD spectra of (a) MXene ($Ti_3C_2T_x$) and (b) $Bi_{1-x}Gd_xFe_{1-y}Sn_y$ (BGFSO)/MXene hybrid samples.

surface area allows more dye molecules to be adsorbed and degraded from an aqueous solution.[10−14]

The two-dimensional (2D) materials having a large surface area play an essential role in overcoming the water pollution challenges. The layered and porous structure of graphene enhances the photocatalytic activity due to the separation of charge carriers and enhanced oxidation and reduction reactions.[15] The hybrid of 2D graphene sheets with TiO_2 nanoparticles showed about 17% higher dye degradation than that from pure TiO_2 nanoparticles.[15−20,52,53] Recently, the nanohybrid of BFO with 2D graphene sheets was reported. Dai et al. reported that 50% degradation efficiency of methyl orange in 6 h can be achieved using the $BiFeO_3$/GO nanohybrid under visible light irradiation.[25] Li et al. synthesized the BFO/GO nanohybrid and reported 48% degradation of colored dye (Congo red) in 120 min by the interaction of visible light with the hybrid surface. Later on, researchers worked out on 2D structures to further improve the degradation efficiency using doped BFO nanoparticles. In 2011, a new family of 2D materials, namely, MXene, was reported, which were more efficient than graphene due to their diversity in structures as well as good conductivity and semiconducting nature.[21−26] They are composed of transition metal carbides and nitrides with different functional groups like OH^-, O^-, and F^- attached on their surface. The general chemical formula of MXene is $M_{n+1}X_nT_x$, where M is the transition metal like titanium, X is carbon, and T_x are the termination groups like OH^-, O^-, and F^-.[24−28] Importantly, there are no reports yet on the doped BFO/MXene nanohybrid, which may be an interesting material candidate for photocatalysis. Keeping this in mind, we have successfully synthesized hybrid samples consisting of Gd^{3+}- and Sn^{4+}-codoped BFO nanoparticles with Ti_3C_2 MXene with varying Sn^{4+} concentrations. The photocatalytic activity of this hybrid for a colored dye (Congo red) is studied under visible light irradiation. The 2D material-based nanohybrids provide a large surface area, narrow band gap, and conductive pathways for charge carriers, resulting in a decrease in the electron−hole recombination, thus becoming promising candidates for photocatalysis application. On the other hand, the gadolinium (Gd^{3+})- and tin (Sn^{4+})-doped bismuth ferrite nanoparticles play an important role in photocatalytic activity due to the mesoporous nature, direct-band-gap semiconductor nature, low band gap, visible-light-active nature, large generation of charge carriers, and long electron−hole recombination time.[29] This work is novel because of its good photocatalytic results, use of new material combination, and excellent catalytic performance. The highest degradation of Congo red dye reported here makes the Gadolinium (Gd^{3+})- and Tin (Sn^{4+})-doped BFO/MXene nanohybrid an excellent photocatalyst under visible light.

2. EXPERIMENTAL DETAILS

2.1. Materials. Bismuth nitrate pentahydrate (99% pure), iron nitrate nonhydrate (98.5% pure), gadolinium nitrate hexahydrate (99.9% pure), and tin powder were used as reactants. Acetic acid (99.5%) was used as a catalyst, and ethylene glycol (99%) was used as a solvent and reducing agent. Hydrofluoric acid (39%) was used for etching of Ti_3AlC_2 MAX powder.

2.2. Synthesis of MXene. For the synthesis of MXene, 10 grams of MAX powder was dispersed in 200 mL of (39%) concentrated hydrofluoric acid in a Teflon bottle. The MAX powder and hydrofluoric acid were mixed together at room temperature through magnetic stirring for up to 36 h. After that, the hot plate was turned off and the solution was left as is for 12 h. The solution was further stirred for 12 h. Finally, the obtained etched powder was washed many times with deionized water and was filtered through the filter paper (Whatman 0.2 mm). The filtrate was dried at 50 °C overnight in a drying oven. The obtained powder was the etched MXene used for fabrication of nanohybrids.[52,53]

2.3. Synthesis of Gd- and Sn-Codoped BFO Nanoparticles. The Gd^{3+}- and Sn^{4+}-codoped BFO nanoparticles (general formula: $Bi_{1-x}Gd_xFe_{1-y}Sn_yO_3$ (x = 0.0, 0.01; y = 0.0, 0.05, 0.10), abbreviated as BGFSO) were prepared by the sol−gel technique. The bismuth nitrate pentahydrate ($Bi(NO_3)_3 \cdot 5H_2O$) and gadolinium nitrate hexahydrate ($Gd(NO_3)_3 \cdot 6H_2O$) powders were added to acetic acid and ethylene glycol used as a solvent solution with a stoichiometric ratio of 1:1 and stirred for 90 min at room temperature. Meanwhile, iron nitrate along with Tin powders was also mixed with acetic acid and stirred for 1.5 h. Then, both these separate solutions were mixed together and were put on a hot plate for 3 h under stirring. A homogeneous reddish-brown solution was obtained, which was dried overnight in a drying oven at 50 °C and further calcined in a hot furnace at a temperature of 600 °C for 3 h.[11]

2.4. Synthesis of MXene Nanohybrids. The nanohybrids of doped BFO with MXene were synthesized using the coprecipitation method. The solution of MXene was prepared in deionized water and sonicated for 10 min. On the other hand, the Sn^{4+}- and Gd^{3+}-doped Bismuth Ferrite nanoparticles ($Bi_{1-x}Gd_xFe_{1-y}Sn_y$: BGFSO) were added into the solution of

DOI: 10.1021/acsomega.8b01951
ACS Omega 2018, 3, 13828−13836

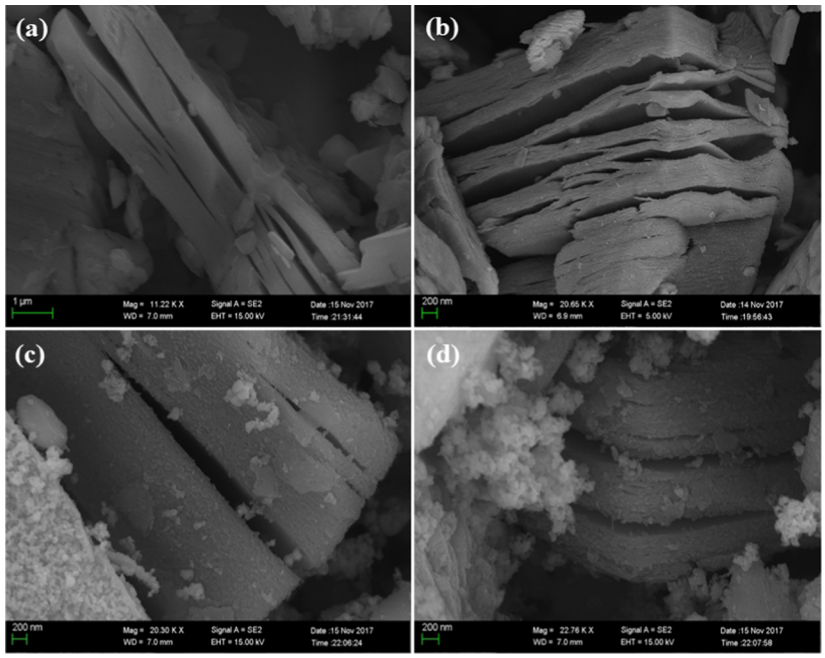

Figure 2. (a, b) Surface morphology of MXene sheets and (c, d) morphology of $Bi_{1-x}Gd_xFe_{1-y}Sn_y$ (BGFSO)/MXene hybrid samples.

acetic acid and ethylene glycol in a ratio of 1:1, molarity of 0.01 M. The prepared solution was sonicated for 2 h at 60 °C. After that, both the solutions were mixed together and stirred for 1 h at 80 °C. The prepared solution was rinsed several times with deionized water and was put in a drying oven at 50 °C for 24 h.

3. RESULTS AND DISCUSSION

3.1. Structural Analysis of Doped BFO Nanoparticles and Nanohybrids. Figure 1a shows the X-ray diffraction (XRD) results of the etched MAX powder known as MXene. The main peaks of MAX are at angles of 9.7 and 19.1° having the (002) and (004) planes, respectively.[52,53] However, the peaks after etching of aluminum are shifted toward lower angles, i.e., at 9.6 and 18.6° having the (002) and (004) planes, respectively. This peak shift toward a lower angle shows an increase in the interplanar distance. The peak intensity of MXene decreases sharply, which indicates the loss of crystalline nature of the MAX powder after aluminum etching as compared to that of the pure unetched MAX compound.[28,29,52,53] The peaks corresponding to the (101) and (105) planes are associated with TiC that might have formed during the formation of MAX as well as during the synthesis of MXene. The XRD patterns of the nanohybrids of $Bi_{0.90}Gd_{0.10}Fe_{0.95}Sn_{0.05}$ (BGFO-5Sn)/MXene, $Bi_{0.90}Gd_{0.10}Fe_{0.90}Sn_{0.10}$ (BGFO-10Sn)/MXene, $Bi_{0.90}Gd_{0.10}Fe_{0.85}Sn_{0.15}$ (BGFO-15Sn)/MXene, and $Bi_{0.90}Gd_{0.10}Fe_{0.80}Sn_{0.20}$ (BGFO-20Sn)/MXene prepared by the coprecipitation method are shown in Figure 1b.

All of the peaks of the doped BFO/MXene nanohybrid are labeled with their corresponding (*hkl*) planes according to the JCPDS card no 20-0169. The pure BFO has a rhombohedral distorted perovskite structure with the *R*3*c* space group at room temperature. With the addition of Sn^{4+} to BFO nanoparticles, the doublet peaks corresponding to the (104) and (110) planes are merged into a single sharp peak, indicating the transformation of structure from rhombohedral to orthorhombic because of difference in the ionic radii of Sn^{4+} (1.09 A°) and Fe^{3+} (0.78 A°) that causes a distortion in the crystal lattice, resulting in the expansion of unit cell volume. With an increase in the doping concentration of Sn^{4+} up to 20%, the peak is shifted toward the lower angle side. This indicates an increase in the interplanar distance and lattice constant because of the replacement of the atom of smaller ionic radii with the atom of larger ionic radii, which produces a tensile stress in the crystal lattice and thus changes the bond length of the unit cell.[9,11] The average crystallite size of prepared nanoparticles ranges from 60 to 20 nm. The dopant atoms that do not move onto the substitutional sites generate crystallinity loss inside the crystal structure and decrease the particle size and are also responsible for broadening of the peaks. The sharp peaks show the crystalline nature of the prepared material. The intensity of the impurity peak of $Bi_2Fe_4O_9$ increases with the increase in doping concentration.[11,54] However, the average crystallite sizes of $Bi_{0.90}Gd_{0.10}Fe_{0.95}Sn_{0.05}$ (BGFO-5Sn)/MXene, $Bi_{0.90}Gd_{0.10}Fe_{0.90}Sn_{0.10}$ (BGFO-10Sn)/MXene, $Bi_{0.90}Gd_{0.10}Fe_{0.85}Sn_{0.15}$ (BGFO-15Sn)/MXene, and $Bi_{0.90}Gd_{0.10}Fe_{0.80}Sn_{0.20}$ (BGFO-20Sn)/MXene nanohybrids are calculated by Scherer's formula ($D = K\lambda/\beta\cos\theta$), and they are found to be 19.72, 21.54, 20.8, and 20.96 nm, respectively. From XRD of hybrid samples, it is clear that the peaks are broadened and have lower intensity due to the presence of etched MXene sheets with doped BFO nanoparticles.[29−32] All of the main peaks of BFO and MXene are present in all hybrid samples, and this is a clear evidence of the successful formation of the hybrid.

3.2. Morphological Analysis. A scanning electron microscope (SEM) was used to study the surface morphology of prepared nanohybrids, as shown in Figure 2. It can be seen that the MXene sheets are layered structures that are flat and smooth with sharp edges (Figure 2a,b), whereas Gd^{3+}- and Sn^{4+}-codoped BFO nanoparticles are dispersed and attached on the surface of MXene sheets, as shown in Figure 2c−g. The attachment of doped BFO nanoparticles on MXene sheets indicates a hybrid formation. However, with the increasing

DOI: 10.1021/acsomega.8b01951
ACS Omega 2018, 3, 13828−13836

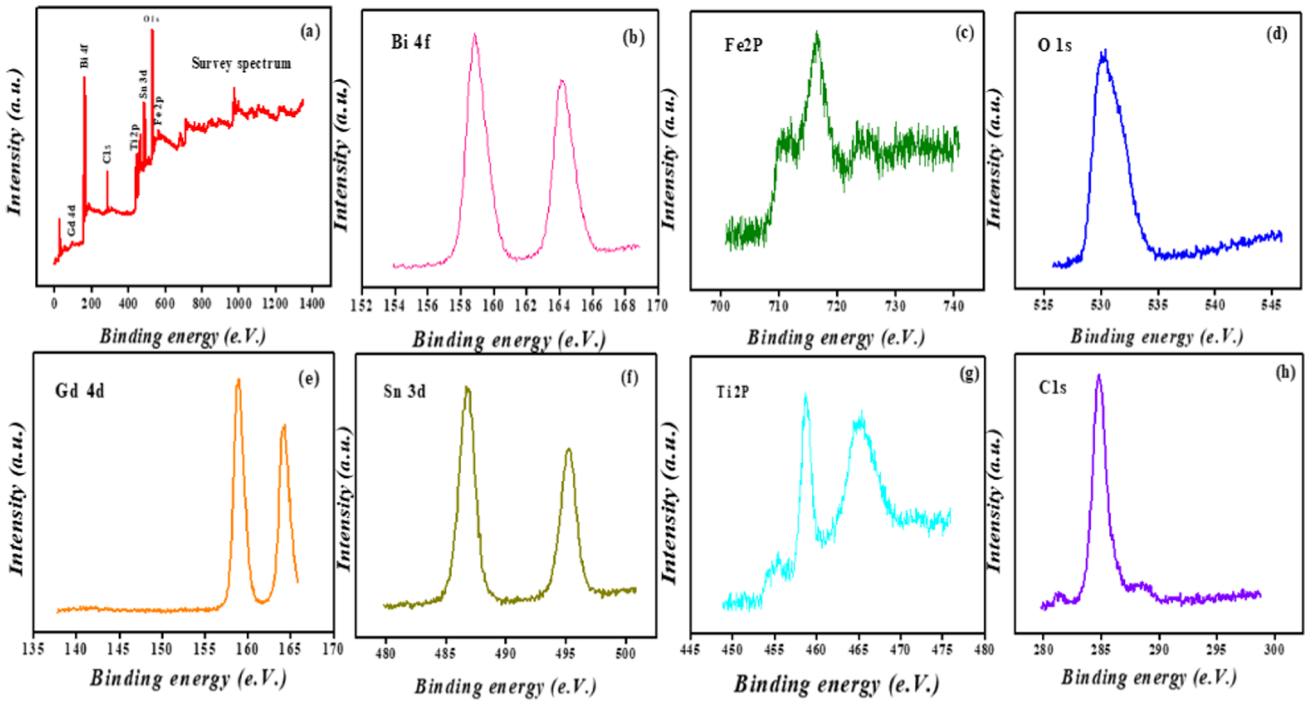

Figure 3. XPS analysis: (a) survey spectrum of $Bi_{1-x}Gd_xFe_{1-y}Sn_y$ (BGFSO)/MXene hybrid samples, (b) Bi 4f core levels, (c) Fe 2p core levels, (d) O 1s core levels, (e) Gd 4d core levels, (f) Sn 3d core levels, (g) Ti 2p core levels, and (h) C 1s core levels.

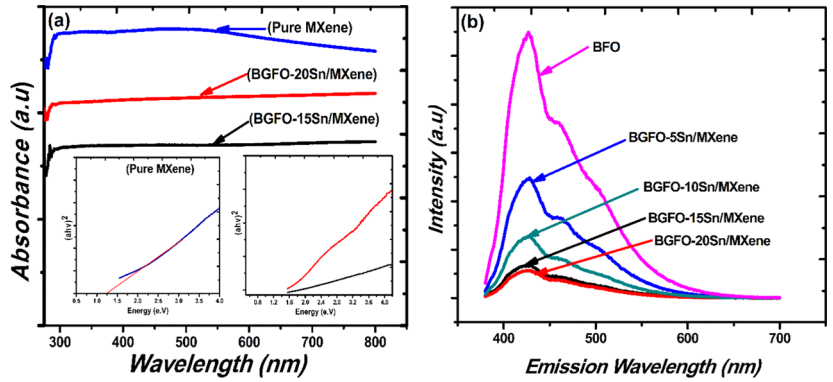

Figure 4. (a) Absorbance and band gap of pure MXene, $Bi_{0.90}Gd_{0.10}Fe_{0.80}Sn_{0.20}$ (BGFO-20Sn)/MXene, and $Bi_{0.90}Gd_{0.10}Fe_{0.85}Sn_{0.15}$ (BGFO-15Sn)/MXene nanohybrid samples. (b) Photoluminescence (PL) spectra of BFO, $Bi_{0.90}Gd_{0.10}Fe_{0.95}Sn_{0.05}$ (BGFO-5Sn)/MXene, $Bi_{0.90}Gd_{0.10}Fe_{0.90}Sn_{0.10}$ (BGFO-10Sn)/MXene, $Bi_{0.90}Gd_{0.10}Fe_{0.85}Sn_{0.15}$ (BGFO-15Sn)/MXene, and $Bi_{0.90}Gd_{0.10}Fe_{0.80}Sn_{0.20}$ (BGFO-20Sn)/MXene.

concentration of Sn^{4+} (5, 10, 15, 20%) in BFO, the metallic nanoparticles agglomerate with each other.

As a result of agglomeration, lesser number of doped BFO nanoparticles are attached onto the MXene sheets while the agglomerated nanoparticles appear in the form of white clusters, as shown in Figure 2c,d. Agglomeration occurs due to the large surface interaction of particles because of a decrease in their size upon doping. Hence, agglomeration of nanoparticles reduces the surface area, making the trapping sites available for dye degradation; thus, it strongly influences the photocatalytic activity.[30,31]

3.3. X-ray Photoelectron (XPS) Spectrum. The XPS spectra provide information about the chemical composition and binding energy of various elements present in the $Bi_{1-x}Gd_xFe_{1-y}Sn_y$ (BGFSO)/MXene nanohybrid. Figure 3 shows XPS analysis of the prepared nanohybrid. The survey spectrum of BGFSO/MXene shown in Figure 3a contains the elemental peaks of Bi, Fe, O, Gd, Sn, Ti, and C present in $Bi_{1-x}Gd_xFe_{1-y}Sn_y$ (BGFSO)/MXene nanohybrids. The two intense peaks of Bi^{3+} corresponding to binding energies of 158.8 and 163.9 eV for Bi $4f_{7/2}$ and Bi $4f_{5/2}$ are shown in Figure 3b.

The peaks positioned at 710 and 716 eV reveal Fe^{3+} oxidation states, and the peak at 724 eV corresponds to Fe_2O_3 (iron oxide) (Figure 3c). The peak at the binding energy of 532 eV corresponds to the O 1s spectrum of the $Bi_{1-x}Gd_xFe_{1-y}Sn_y$ (BGFSO)/MXene nanohybrid. This peak arises due to the absorbed oxygen atoms into the solution from the atmosphere, as shown in Figure 3d. The spectrum of C 1s at the binding energy of 284.8 eV indicates the C−O bonding. Also, there is no existence of C−Fe and C−C emission peaks in Figure 3h.[32] The peak at 464 eV demonstrates the presence of Ti−O bonding, and the peak at 459 eV corresponds to the Ti^{4+} oxidation state that is described in Figure 3g.[30,34,35,52,53] The intense peak located at the binding energy of 494 eV is the $3d_{3/2}$ state of Sn^{4+}, whereas the two small peaks of Gd^{3+} at

DOI: 10.1021/acsomega.8b01951
ACS Omega 2018, 3, 13828−13836

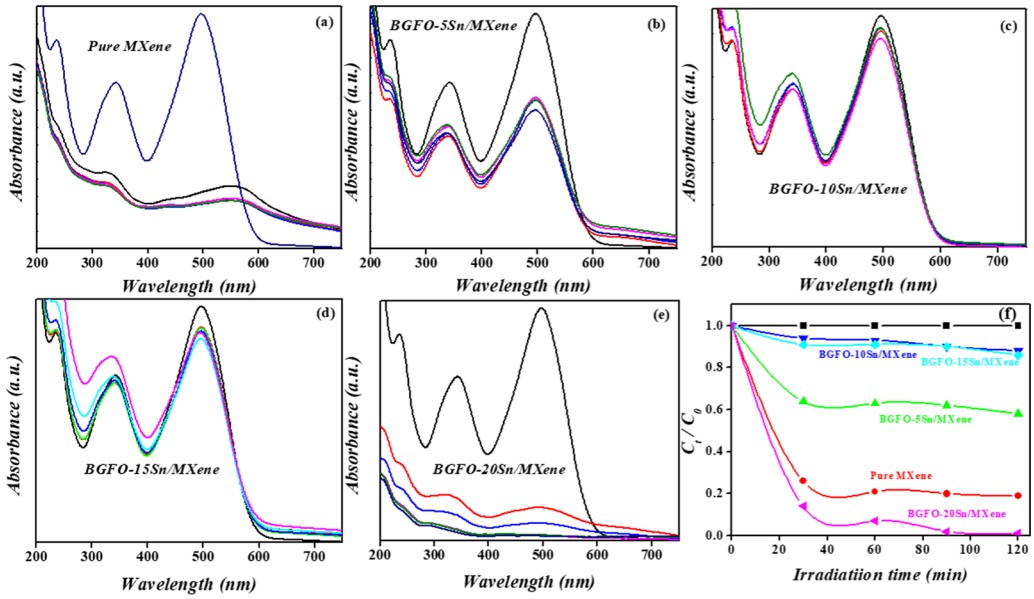

Figure 5. (a–e) Absorbance spectra of MXene, $Bi_{0.90}Gd_{0.10}Fe_{0.95}Sn_{0.05}$ (BGFO-5Sn)/MXene, $Bi_{0.90}Gd_{0.10}Fe_{0.90}Sn_{0.10}$ (BGFO-10Sn)/MXene, $Bi_{0.90}Gd_{0.10}Fe_{0.85}Sn_{0.15}$ (BGFO-15Sn)/MXene, and $Bi_{0.90}Gd_{0.10}Fe_{0.80}Sn_{0.20}$ (BGFO-20Sn)/MXene. (f) Photocatalytic degradation of pure MXene, $Bi_{0.90}Gd_{0.10}Fe_{0.95}Sn_{0.05}$ (BGFO-5Sn)/MXene, $Bi_{0.90}Gd_{0.10}Fe_{0.90}Sn_{0.10}$ (BGFO-10Sn)/MXene, $Bi_{0.90}Gd_{0.10}Fe_{0.85}Sn_{0.15}$ (BGFO-15Sn)/MXene, and $Bi_{0.90}Gd_{0.10}Fe_{0.80}Sn_{0.20}$ (BGFO-20Sn)/MXene.

binding energies of 158 eV and 164 eV correspond to $3d_{3/2}$ and $3d_{5/2}$ states, respectively, as shown in Figure 3e,f.[9] From XPS results, it can be predicted that the atoms in the prepared hybrid samples do not show a chemical bonding, i.e., ionic and covalent bonds and hence no chemical shift takes place during hybrid formation.

3.4. Optical Properties of Nanohybrid. The optical properties of hybrid samples are investigated using a UV–visible spectrophotometer. The absorbance spectra of pure MXene, $Bi_{0.90}Gd_{0.10}Fe_{0.85}Sn_{0.15}$ (BGFO-15Sn)/MXene, and $Bi_{0.90}Gd_{0.10}Fe_{0.80}Sn_{0.20}$ (BGFO-20Sn)/MXene hybrids show the absorbance of light in the visible region (400–800 nm), as can be seen in Figure 4a, which is a clear indication that the pure MXene and doped $Bi_{1-x}Gd_xFe_{1-y}Sn_y$ (BGFSO) hybrid samples continuously absorb light. Hence, there is no absorption edge originating in pure MXene and doped BFO/MXene hybrid samples due to the metallic properties of MXene that arise because of partial etching of aluminum from MAX powder.[52,55] Moreover, the atoms of Bi, Fe, and O do not penetrate into MXene sheets as they just undergo surface adsorption phenomena on MXene; as a result, there is no absorption edge in hybrid samples because of the metallic nature of MXene.[55] The band gap of MXene, $Bi_{0.90}Gd_{0.10}Fe_{0.85}Sn_{0.15}$ (BGFO-15Sn)/MXene, and $Bi_{0.90}Gd_{0.10}Fe_{0.80}Sn_{0.20}$ (BGFO-20Sn)/MXene hybrid samples was calculated using Tauc's plot

$$(\alpha h\nu) = A(h\nu - E_g)^n \quad (1)$$

whereas A is a constant, h is Planck's constant, ν is the frequency of irradiated light, E_g is the band gap energy, and α is the absorbance of light.[33] The band gap of hybrid samples was obtained by plotting $(\alpha h\nu)^2$ against band gap energy E_g.[34−3834−38] The band gaps of $Bi_{0.90}Gd_{0.10}Fe_{0.85}Sn_{0.15}$ (BGFO-15Sn)/MXene and $Bi_{0.90}Gd_{0.10}Fe_{0.80}Sn_{0.20}$ (BGFO-20Sn)/MXene were found to be 1.6 and 1.4 eV, respectively, as shown in Figure 4.[36,39] This reduction in the band gap of hybrid samples was observed due to the incorporation of stacked and porous MXene sheets into doped BFO nanoparticles, which develop intermediate states between the conduction band (CB) and the valence band (VB) of doped BFO nanoparticles across the interface, which causes reduction in the band gap.[11,37,38,40,52,53]

3.5. Photoluminescence Emission Spectrum. Photoluminescence (PL) emission spectrum was used to determine the electron–hole recombination rate. The photoluminescence spectra contain a central peak at 426 nm and a shoulder peak at 458 nm. The shoulder peak originates due to the presence of defects and impurity energy levels in the prepared samples.[44−47] These defects arise in the hybrid samples due to the partial etching of aluminum from the MAX powder and may also appear during doping BFO by Gd^{3+} and Sn^{4+} elements.[11] The central peak appearing at 426 nm shows the recombination rate of charge carriers; the greater the electron–hole recombination rate, the greater the PL peak intensity and vice versa.[41−46] Figure 4b shows the PL emission spectra of doped BFO/MXene hybrid samples. The $Bi_{0.90}Gd_{0.10}Fe_{0.80}Sn_{0.20}$ (BGFO-20Sn)/MXene and $Bi_{0.90}Gd_{0.10}Fe_{0.85}Sn_{0.15}$ (BGFO-15Sn)/MXene samples have small PL peak intensities that correspond to a lower electron–hole recombination rate than that for BFO/MXene, $Bi_{0.90}Gd_{0.10}Fe_{0.95}Sn_{0.05}$ (BGFO-5Sn)/MXene, and $Bi_{0.90}Gd_{0.10}Fe_{0.90}Sn_{0.10}$ (BGFO-10Sn)/MXene. This is because of the porous 2D MXene sheets that trap the electrons and enhance the electron–hole separation. The lower recombination of charge carriers provides efficient dye degradation and thus enhances the photocatalytic activity.[47,48]

3.6. Photocatalytic Activity. The photocatalytic activity of doped BFO hybrid samples for degradation of Congo red is shown in Figure 5. For this purpose, two experiments were performed in dark and light. In the dark experiment, Congo red was added into the catalytic solution under no light. As a result, no dye degradation takes place because of no generation of charge carriers i.e., electrons and holes. The dark effect is significant and is due to adsorption, which is unavoidable. The

DOI: 10.1021/acsomega.8b01951
ACS Omega 2018, 3, 13828−13836

experiment that took place under light plays an important role in dye degradation because of the formation of charge carriers.

In the light experiment, 100 mg of hybrid samples (catalyst) was added into the Congo red dye solution (100 mL). A Xenon lamp having a power of 300 W was used as a visible light source for a wavelength range of 400−700 nm. During the experiment, the solution was stirred continuously so that the sample and the dye molecules mixed equally into the water. Then, 5 mL solution was taken out after every 30 min and was centrifuged to check for supernatant by a UV−vis spectrometer to analyze dye degradation from the solution. Meanwhile, the degradation of dye can also be observed by discharge of color from the catalytic solution. This discharge of dye color is because of the breakdown of the azo bonds between the dye molecules. The dye degradation efficiency can be determined using the following equation

$$\text{degradation (\%)} = \frac{C_o - C}{C_o} \times 100 \quad (2)$$

whereas C_o is the initial concentration of dye solution and C is the concentration of dye solution at any time t.[11,45,47,49−51] The absorbance spectra of all of the hybrid samples and pure MXene are shown in Figure 5a−e The absorbance spectra of pure MXene at different times indicate the concentration of Congo red dye as well as its degradation efficiency from the catalytic solution.[11] The MXene sheets are black, indicating that the sheets absorb all types of radiation (UV, vis, and NIR). The red peak at high intensity shows the highest concentration of dye molecules into the solution. As the time goes on, the concentration of dye molecules decreases; hence, less light absorption takes place due to less interaction of it with molecules and a decrease in the absorption peak intensity occurs with time.[60] The decrease in the intensity of absorbance peak with time is a clear evidence of dye degradation from the catalytic solution. However, in the case of pure MXene catalyst, after 30 min, the absorbance peak is shifted toward the longer-wavelength region because of the attachment of a large number of oxygen atoms onto the MXene surface that oxidizes the sheets as $Ti_3C_2O_2$.[56−59] The peak that is shifted at above 500 nm may be due to the presence of dye molecules that are smaller in size and require less amount of energy for transitions to higher energy levels, so the lesser the energy, the higher the wavelength, and this is the reason for peak shift.[60,61]

The absorbance of dye over the catalyst surface is strongly related to the degradation rate of Congo red dye from the photocatalytic solution. From Figure 5f, it can be observed that the black line corresponds to the degradation of Congo red from solution without light irradiation. Moreover, 80% Congo red dye is degraded from the pure MXene solution in 120 min, which is a clear evidence that the MXene sheet has a good photocatalytic activity due to its larger surface area and porous nature. $Bi_{0.90}Gd_{0.10}Fe_{0.95}Sn_{0.05}$ (BGFO-5Sn)/MXene degraded 38% of dye solution, whereas 18% dye degradation took place from $Bi_{0.90}Gd_{0.10}Fe_{0.90}Sn_{0.10}$ (BGFO-10Sn)/MXene and $Bi_{0.90}Gd_{0.10}Fe_{0.85}Sn_{0.15}$ (BGFO-15Sn)/MXene in 120 min. $Bi_{0.90}Gd_{0.10}Fe_{0.80}Sn_{0.20}$ (BGFO-20Sn)/MXene is a good photocatalyst because of 100% dye degradation in 120 min. This shows that the doped BFO/MXene hybrid samples have a good photocatalytic activity in the presence of light rather than under dark conditions.

Here, of all of the prepared hybrid samples, the $Bi_{0.90}Gd_{0.10}Fe_{0.80}Sn_{0.20}$ (BGFO-20Sn)/MXene hybrid sample is the best photocatalyst due to its small average particle size (19 nm) as well as its band gap being tuned to 1.5 eV and low electron−hole recombination rate as compared to those for other counterparts. The tuned band gap and low electron−hole recombination are due to the incorporation of MXene sheets into the doped BFO nanoparticles. Because of the porous nature and large surface area, MXene sheets trap the charges and enhance the separation of charges, i.e., holes and electrons.[55] On the other hand, because of the mesoporous nature, BGFO-20Sn also traps a large number of dye molecules as the sizes of doped BFO nanoparticles and Congo red dye molecules are comparable, which enhances their degradation activity. At a higher doping concentration, the enhanced photocatalytic activity is also because of the large number of active sites available on the photocatalyst surface that are produced due to the presence of a large number of defects. These defects make the material more reactive to the charge carriers and the functional groups (OH^-, F^-, O^-) attached on MXene thus produce radicals that further help in promoting dye degradation.[11,29,32,52,55]

Another factor that helps faster degradation of dye is the pH of the $Bi_{0.90}Gd_{0.10}Fe_{0.80}Sn_{0.20}$ (BGFO-20Sn)/MXene hybrid sample as well as the pure MXene sample. The pH of the $Bi_{0.90}Gd_{0.10}Fe_{0.80}Sn_{0.20}$ (BGFO-20Sn)/MXene sample was 2, whereas the pH of the pure MXene sample was 3. The greater the pH of the solution, the greater the concentration of H^+ ions in the solution and so the higher the positive charges on the catalyst surface as the dye molecules carry a negative charge because of the presence of functional groups. Thus, more electrostatic attraction develops between them. As a result, more adsorption of dye molecules occurs on the photocatalyst surface. Therefore, the greater the adsorption of dye molecules, the larger the degradation.[53−57] Moreover, the pH of the MXene solution is 3; thus, the concentration of H^+ molecules will be lesser in the solution, which indicates less positive charge on the catalyst surface and less electrostatic interaction between the catalyst and dye molecules. Hence, the degradation rate of Congo red will be lower in the case of pure MXene than in $Bi_{0.90}Gd_{0.10}Fe_{0.80}Sn_{0.20}$ (BGFO-20Sn)/MXene.[53,55,56]

3.7. Proposed Photocatalytic Mechanism. The mechanism of photocatalysis is based on the oxidation and reduction reactions occurred on the nanohybrid surface in the presence of electrons and holes. The electrons and holes are generated due to the interaction of visible light with the catalyst surface, which produces radical ions. When electrons undergo the reduction reaction with oxygen and holes undergo the oxidation reaction with water, the OH^- and O_2^- radicals are produced. These radicals are highly reactive species for the degradation of Congo red dye from water and give harmless end products like CO_2 and H_2O.

These harmless products can further be reduced to get hydrocarbons like methane, etc. Figure 6 shows the proposed photocatalytic mechanism for dye degradation. Charge generation takes place when light interacts with the catalyst surface (eq 3). MXene sheets act as acceptors as they trap electrons and enhance the separation of charge carriers (eq 4). Electrons react with adsorbed oxygen, O_2, to undergo the reduction reaction and convert oxides into superoxide radicals, O_2^-; holes react with water molecules and are oxidized into hydroxyl radical ions, OH^- (eqs 5 and 6). These species react with Congo red dye and degrade it from the catalytic solution to give harmless end products like H_2O and CO_2.[45,46,61]

DOI: 10.1021/acsomega.8b01951
ACS Omega 2018, 3, 13828−13836

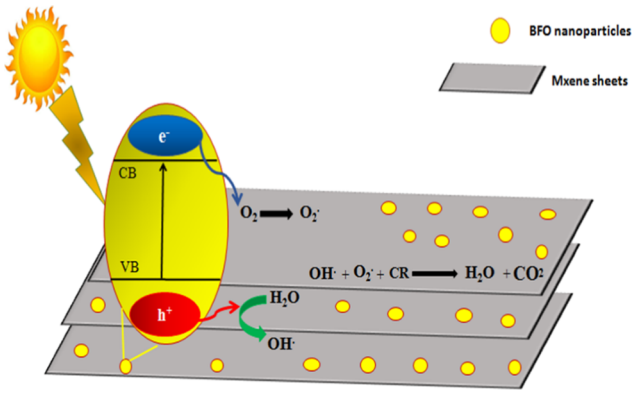

Figure 6. Doped BFO/MXene nanohybrid Congo red (CR) dye degradation mechanism.

The proposed photocatalytic degradation mechanism is expressed by the following equations[45,61]

$$\text{BGFSO} - \text{MXene} + h\nu \rightarrow \text{BGFSO}\ (e^- + h^+) \quad (3)$$

$$e^- + \text{MXene} \rightarrow e^-\ (\text{MXene trapped electrons}) \quad (4)$$

$$e^-\ (\text{MXene trapped electrons}) + O_2 \rightarrow^{\bullet} O_2^- \quad (5)$$

$$h^+ + H_2O \rightarrow^{\bullet} OH^- \quad (6)$$

$$\bullet OH^- + CR \rightarrow CO_2 + H_2O \quad (7)$$

$$\bullet O_2^- + CR \rightarrow CO_2 + H_2O \quad (8)$$

It can be seen that $Bi_{0.90}Gd_{0.10}Fe_{0.80}Sn_{0.20}$ (BGFO-20Sn)/MXene is a good photocatalyst. The enhanced photocatalytic activity is because of the short electron−hole recombination time, low band gap (1.4 eV), and small crystallite size as compared to those for other nanohybrid samples. The low band gap is because of gadolinium (Gd^{3+}) and tin (Sn^{4+}) doping that further generates more number of electrons and holes and thus more production of OH^- and O_2^- radicals by oxidation and reduction reactions, respectively. Hence, more production of OH^- and O_2^- radicals allow more degradation of organic pollutants from water.[61]

4. CONCLUSIONS

The $Bi_{1-x}Gd_xFe_{1-y}Sn_y$ (BGFSO)/MXene nanohybrids were synthesized by the coprecipitation method. The XRD and SEM results clearly indicate the formation of $Bi_{1-x}Gd_xFe_{1-y}Sn_y$ (BGFSO)/MXene nanohybrids. The incorporation of MXene sheets into BGFSO nanoparticles reduces their band gap due to the porous nature of MXene sheets that helps trap the charge particles and reduce their recombination rate. The band gap of nanohybrids is also reduced due to the conducting nature of the 2D MXene surface. The XPS results also indicate successful formation of the nanohybrid rather than their chemical interaction. The degradation rate of Congo red dye from the catalytic solution is higher in the case of $Bi_{0.90}Gd_{0.10}Fe_{0.80}Sn_{0.20}$ (BGFO-20Sn)/MXene, showing 100% degradation of dye from the catalytic solution, than that for $Bi_{0.90}Gd_{0.10}Fe_{0.95}Sn_{0.05}$ (BGFO-5Sn)/MXene, showing 38% degradation along with 18% dye degradation for $Bi_{0.90}Gd_{0.10}Fe_{0.90}Sn_{0.10}$ (BGFO-10Sn)/MXene and $Bi_{0.90}Gd_{0.10}Fe_{0.85}Sn_{0.15}$ (BGFO-15Sn)/MXene. The good photocatalytic result of $Bi_{0.90}Gd_{0.10}Fe_{0.80}Sn_{0.20}$ (BGFO-20Sn)/MXene was due to the small crystallite size (19 nm), which is attributed to the higher surface area and low band gap. The present catalyst is reported for the first time with the highest (100%) dye-degradation efficiency in 2 h at room temperature, fabricated using a simple and cost-effective route and thus is suitable for industrial application.

AUTHOR INFORMATION

Corresponding Author

*E-mail: syedrizwanh83@gmail.com. Tel: +92-9085-5599.

ORCID

S. Irfan Ali: 0000-0002-6015-2415

Notes

The authors declare no competing financial interest.

ACKNOWLEDGMENTS

The higher education commission (HEC) of Pakistan funded the research activity under the 6040/Federal/NRPU/R&D/HEC/2015 to carry out the research work within Pakistan.

REFERENCES

(1) Cui, W.; Li, J.; Sun, Y. Enhancing ROS Generation and Suppressing Toxic Intermediate Production in Photocatalytic NO Oxidation on O/Ba Co-Functionalized Amorphous Carbon Nitride. *Appl. Catal., B* **2018**, *237*, 938−946.

(2) Raffainer, I. I.; Rudolf von Rohr, P. Promoted wet Oxidation of the Azo Dye Orange II under Mild Conditions. *Ind. Eng. Chem. Res.* **2001**, *40*, 1083−1089.

(3) Ramsay, R. R.; Dunford, C.; Gillman, P. K. Methylene blue and serotonin toxicity: inhibition of monoamine oxidase A (MAO A) confirms a theoretical prediction. *Br. J. Pharmcol.* **2007**, *152*, 946−951.

(4) Afkhami, A.; Moosavi, R. Adsorptive removal of Congo red, a carcinogenic textile dye, from aqueous solutions by maghemite nanoparticles. *J. Hazard. Mater.* **2010**, *174*, 398−403.

(5) Kobylewski, S.; Jacobson, M. F. Enhanced Photocatalytic Properties of Visible Light Responsive La/TiO_2−Graphene Composites for the Removal of Rhodamin B in Water. *Adv. Electron. Electr. Eng.* **2012**, *18*, 220−246.

(6) Prihod'ko, R. V.; Soboleva, N. M. Photocatalysis: Oxidative Processes in Water Treatment. *J. Chem.* **2013**, *29*, 1−8.

(7) Wang, H.; Sun, Y.; Jiang, Y.; Huang, H.; Wu, Z.; Lee, S.; Dong, F. Efficient and stable photocatalytic NO removal on C self-doped g-C_3N_4: Electronic structure and reaction mechanism. *Environ. Sci. Technol.* **2018**, *52*, 1479−1487.

(8) Vijayan, B. K.; Dimitrijevic, N. M.; Wu, J.; Gray, K. A. Preparation of Improved p-n Junction NiO/TiO_2 Nanotubes for Solar-Energy-Driven Light Photocatalysis. *J. Phys. Chem. C* **2010**, *114*, 21262−21269.

(9) Shu, X.; He, J.; Chen, D. Visible-Light-Induced Photocatalyst Based on Nickel Titanate Nanoparticles. *Ind. Eng. Chem. Res.* **2008**, *47*, 4750−4753.

(10) Asahi, R.; Morikawa, T.; Ohwaki, T.; Aoki, K.; Taga, Y. Visible-Light Photocatalysis in Nitrogen-Doped Titanium Oxides. *Science* **2001**, *293*, 269−271.

(11) Irfan, S.; Rizwan, S.; Shen, Y.; Li, L.; Asfandiyar, A.; Butt, S.; Nan, W. The Gadolinium (Gd^{3+}) and Tin (Sn^{4+}) Co-doped $BiFeO_3$ Nanoparticles as New Solar Light Active Photocatalyst. *Sci. Rep.* **2017**, *2*, No. 42493.

(12) Sun, B.; Wei, L.; Li, H.; Chen, P. White-light-controlled ferromagnetic and ferroelectric properties of multiferroic single-crystalline $BiFeO_3$ nanoflowers at room temperature. *J. Mater. Chem. C* **2014**, *2*, 7547−7551.

(13) Li, Z.; Shen, Y.; Yang, C.; Lei, Y.; Guan, Y.; Lin, Y.; Liu, D.; Nan, C.-W. Significant enhancement in the visible light photocatalytic properties of $BiFeO_3$−Graphene nanohybrids. *J. Mater. Chem. A* **2013**, *1*, 823−829.

DOI: 10.1021/acsomega.8b01951
ACS Omega 2018, 3, 13828−13836

(14) Wang, N.; Zhu, L.; Lei, M.; She, Y.; Cao, M.; Tang, H. Ligand-Induced Drastic Enhancement of Catalytic Activity of Nano-$BiFeO_3$ for Oxidative Degradation of Bisphenol A. *ACS Catal.* **2011**, *1*, 1193−1202.
(15) Li, Y.; Sun, Y.; Ho, W.; Zhang, Y.; Huang, H.; Cai, Q.; Dong, F. Highly enhanced visible-light photocatalytic NO_x purification and conversion pathway on self-structurally modified g-C_3N_4 Nanosheets. *Sci. Bull.* **2018**, *63*, 609−620.
(16) Yoo, J. J.; Balakrishnan, K.; Huang, J.; Meunier, V.; Sumpter, B. G.; Srivastava, A.; Conway, M.; Mohana Reddy, A. L.; Yu, J.; Vajtai, R. Ultrathin planar Graphene supercapacitors. *Nano Lett.* **2011**, *11*, 1423−1427.
(17) Schwierz, F. Graphene Transistors. *Nat. Nanotechnol.* **2010**, *5*, No. 487.
(18) Fowler, J. D.; Allen, M. J.; Tung, V. C.; Yang, Y.; Kaner, R. B.; Weiller, B. H. Practical chemical sensors from chemically derived graphene. *ACS Nano* **2009**, *3*, 301−306.
(19) Bizeto, M. A.; Shiguihara, A. L.; Constantino, V. R. Layered Niobate Nanosheets: building blocks for advanced materials assembly. *J. Mater. Chem.* **2009**, *19*, 2512−2525.
(20) Stoller, M. D.; Park, S.; Zhu, Y.; An, J.; Ruoff, R. S. Graphene-based ultra-capacitors. *Nano Lett.* **2008**, *8*, 3498−3502.
(21) Stankovich, S.; Dikin, D. A.; Dommett, G. H.; Kohlhaas, K. M.; Zimney, E. J.; Stach, E. A.; Piner, R. D.; Nguyen, S. T.; Ruoff, R. S. Graphene based Composite materials. *Nature* **2006**, *442*, No. 282.
(22) Novoselov, K. S.; Jiang, D.; Schedin, F.; Booth, T.; Khotkevich, V.; Morozov, S.; Geim, A. Two dimensional atomic crystal. *Proc. Natl. Acad. Sci. U.S.A.* **2005**, *102*, 10451−10453.
(23) Dai, J.; Xian, T.; Di, L.; Yang, H. Preparation of $BiFeO_3$-Graphene Nanocomposites and their Enhanced Photocatalytic Activities. *J. Nanomater.* **2013**, *20*, 131.
(24) Anasori, B.; Xie, Y.; Beidaghi, M.; Lu, J.; Hosler, B. C.; Hultman, L.; Kent, P. R.; Gogotsi, Y.; Barsoum, M. W. Two-Dimensional, Ordered, Double Transition Metals Carbides (MXenes). *ACS Nano* **2015**, *9*, 9507−9516.
(25) Khazaei, M.; Arai, M.; Sasaki, T.; Chung, C. Y.; Venkataramanan, N. S.; Estili, M.; Sakka, Y.; Kawazoe, Y. Novel electronic and magnetic properties of two dimensional transition metal carbides and nitrides. *Adv. Funct. Mater.* **2013**, *23*, 2185−2192.
(26) Naguib, M.; Kurtoglu, M.; Presser, V.; Lu, J.; Niu, J.; Heon, M.; Hultman, L.; Gogotsi, Y.; Barsoum, M. W. Two-dimensional Nanocrystals produced by exfoliation of Ti_3AlC_2. *Adv. Mater.* **2011**, *23*, 4248−4253.
(27) Khazaei, M.; Arai, M.; Sasaki, T.; Estili, M.; Sakka, Y. Two dimensional Molybdenum carbides, potential thermoelectric materials of the MXene family. *Phys. Chem. Chem. Phys.* **2014**, *16*, 7841−7849.
(28) Kurtoglu, M.; Naguib, M.; Gogotsi, Y.; Barsoum, M. W. First principles study of two-dimensional early transition metal carbides. *MRS Commun.* **2012**, *2*, 133−137.
(29) Dong, X.; Li, J.; Xing, Q.; Zhou, Y.; Huang, H.; Dong, F. The activation of reactants and intermediates promotes the selective photocatalytic NO conversion on electron-localized Sr-intercalated g-C_3N_4. *Appl. Catal., B* **2018**, *232*, 69−76.
(30) Naguib, M.; Mashtalir, O.; Carle, J.; Presser, V.; Lu, J.; Hultman, L.; Gogotsi, Y.; Barsoum, M. W. Two Dimensional Transition metal carbides. *ACS Nano* **2012**, *6*, 1322−1331.
(31) Naguib, M.; Kurtoglu, M.; Presser, V.; Lu, J.; Niu, J.; Heon, M.; Hultman, L.; Gogotsi, Y.; Barsoum, M. W. Two-dimensional Nanocrystals produced by exfoliation of Ti_3AlC_2. *Adv. Mater.* **2011**, *23*, 4248−4253.
(32) Singh, S.; Ishiwara, H.; Maruyama, K. Room temperature ferroelectric properties of Mn-substituted $BiFeO_3$ thin films deposited on Pt electrodes using chemical solution deposition. *Appl. Phys. Lett.* **2006**, *88*, No. 262908.
(33) Ma, Z.; Hu, Z.; Zhao, X.; Tang, Q.; Wu, D.; Zhou, Z.; Zhang, L. Tunable Band Structures of Heterostructured Bilayers with Transition-Metal Dichalcogenide and MXene Monolayer. *J. Phys. Chem. C* **2014**, *118*, 5593−5599.
(34) Zou, G.; Zhang, Z.; Guo, J.; Liu, B.; Zhang, Q.; Fernandez, C.; Peng, Q. Synthesis of Nano flower-Shaped MXene Derivative with Unexpected Catalytic Activity for Dehydrogenation of Sodium Alanates. *ACS Appl. Mater. Interfaces* **2016**, *8*, 22280−22286.
(35) Zhang, Z.; Li, H.; Zou, G.; Fernandez, C.; Hu, J.; Liu, B.; Zhang, Q.; Peng, Q. Self-Reduction Synthesis of New MXene/Ag Composites with Unexpected Electrocatalytic Activity. *ACS Sustainable Chem. Eng.* **2016**, *12*, 6763−6771.
(36) Myhra, S.; Crossley, J.; Barsoum, M. Crystal-chemistry of the Ti_3AlC_2 and Ti_4AlN_3 layered carbide/nitride phases—characterization by XPS. *J. Phys. Chem. Solids* **2001**, *62*, 811−817.
(37) Munk, F.; Kubelka, P. Ein Beitrag Zur Optik Der Farbanstriche. *Z. Tech. Phys.* **1931**, *12*, 593−601.
(38) Xu, X.; Lin, Y. H.; Li, P.; Shu, L.; Nan, C. W. Synthesis and Photocatalytic Behaviors of High Surface Area BiFeO3 Thin Films. *J. Am. Ceram. Soc.* **2011**, *94*, 2296−2299.
(39) Butler, M. Photoelectrolysis and physical properties of the semiconducting electrode WO_2. *J. Appl. Phys.* **1977**, *48*, 1914−1920.
(40) Gao, F.; Chen, X.; Yin, K.; Dong, S.; Ren, Z.; Yuan, F.; Yu, T.; Zou, Z.; Liu, J. M. Visible-Light Photocatalytic Properties of Weak Magnetic $BiFeO_3$ Nanoparticles. *Adv. Mater.* **2007**, *19*, 2889−2892.
(41) Guo, R.; Fang, L.; Dong, W.; Zheng, F.; Shen, M. Enhanced Photocatalytic Activity and Ferromagnetism in Gd Doped $BiFeO_3$ Nanoparticles. *J. Phys. Chem. C* **2010**, *114*, 21390−21396.
(42) Joshi, U. A.; Jang, J. S.; Borse, P. H.; Lee, J. S. Microwave synthesis of single-crystalline perovskite $BiFeO_3$ Nanocubes for photoelectrode and photocatalytic applications. *Appl. Phys. Lett.* **2008**, *92*, No. 242106.
(43) Xu, H.-M.; Wang, H.-C.; Shen, Y.; Lin, Y.-H.; Nan, C.-W. Photocatalytic and magnetic behaviors of $BiFeO_3$ thin films deposited on different substrates. *J. Appl. Phys.* **2014**, *116*, No. 174307.
(44) Wang, X.; Mao, W.; Wang, Q.; Zhu, Y.; Min, Y.; Zhang, J.; Yang, T.; Yang, J.; Li, X.; Huang, W. Low-temperature fabrication of $Bi_{25}FeO_{40}$/RGO nanocomposites with efficient photocatalytic performance under visible light irradiation. *RSC Adv.* **2017**, *7*, 10064−10069.
(45) Soltani, T.; Lee, B.-K. Sono-synthesis of nanocrystallized $BiFeO_3$/Reduced graphene oxide composites for visible photocatalytic degradation improvement of bisphenol A. *Chem. Eng. J.* **2016**, *306*, 204−213.
(46) Irfan, S.; Shen, Y.; Rizwan, S.; Wang, H. C.; Khan, S. B.; Nan, C. W. Band-Gap Engineering and Enhanced Photocatalytic Activity of Sm and Mn Doped $BiFeO_3$ Nanoparticles. *J. Am. Ceram. Soc.* **2017**, *100*, 31−40.
(47) Irfan, S.; Li, L.; Saleemi, A.; Nan, C. W. Enhanced photocatalytic activity of La^{3+} and Se^{4+} co-doped bismuth ferrite nanostructures. *J. Mater. Chem. A* **2017**, *5*, 11143−11151.
(48) Liqiang, J.; Yichun, Q.; Baiqi, W.; Shudan, L.; Baojiang, J.; Libin, Y.; Wei, F.; Honggang, F.; Jiazhong, S. Review of photoluminescence performance of nano-sized semiconductor materials and its relationships with photocatalytic activity. *Sol. Energy Mater. Sol. Cells* **2006**, *90*, 1773−1787.
(49) Di, L.; Yang, H.; Xian, T.; Chen, X. Enhanced Photocatalytic Activity of $NaBH_4$ Reduced $BiFeO_3$ Nanoparticles for Rhodamine B Decolorization. *Materials* **2017**, *10*, No. 1118.
(50) Shafiqul, M.; Khanom, R.; Arifur, M. Removal of Congo Red Dye from Industrial Wastewater by Untreated Sawdust. *Am. J. Environ. Prot.* **2015**, *4*, 207−213.
(51) Naraghi, B.; Zabihi, F.; Reza, M.; Saeidi, M.; Biglari, H. Removal of Acid Orange 7 dye from aqueous solutions by adsorption onto Kenya tea pulps; granulated shape. *Electron. Physician* **2017**, *9*, 4312−4321.
(52) Peng, C.; Yang, X.; Li, Y.; Yu, H.; Wang, H.; Peng, F. Hybrids of Two-Dimensional Ti_3C_2 and TiO_2 Exposing {001} Facets toward Enhanced Photocatalytic Activity. *ACS Appl. Mater. Interfaces* **2016**, *8*, 7607−8322.
(53) Gao, Y.; Wang, L.; Zhou, A.; Li, Z.; Chen, J.; Bala, H.; Hu, Q.; Cao, X. Hydrothermal synthesis of TiO_2/Ti_3C_2 nanocomposites with enhanced photocatalytic activity. *Mater. Lett.* **2015**, *150*, 62−64.

DOI: 10.1021/acsomega.8b01951
ACS Omega 2018, 3, 13828−13836

(54) Sharma, K.; Singh, A. Process in the Growth and characterization of Nano-structured Bismuth Ferrite Thin Films. *J. Adv. Chem. Sci.* **2016**, *2*, 219−222.
(55) Ran, J.; Gao, G.; Li, F. T.; Ma, T. Y.; Du, A.; Qiao, S. Ti_3C_2 MXene co-catalyst on metal sulfide photo-absorbers for enhanced visible-light photocatalytic hydrogen production. *Nat. Commun.* **2017**, *8*, No. 13907.
(56) Persson, I.; Naslund, L.; Halim, J.; Barsoum, M.; Darakchieva, V.; Palisaitis, J.; Rosen, J. On the organization and thermal behavior of functional groups on Ti_3C_2 MXene surfaces in vacuum. *2D Mater.* **2017**, *5*, No. 015002.
(57) Satheeshkumar, E.; Makaryan, T.; Melikyan, A.; Minassian, H.; Gogotsi, Y.; Yoshimura, M. One-step Solution Processing of Ag, Au and Pd @ MXene Hybrids for SERS. *Sci. Rep.* **2016**, *6*, No. 32049.
(58) Berdiyorov, G. R. Optical properties of functionalized $Ti_3C_2T_2$ (T = F, O, OH) MXene: First-principles calculations. *AIP Adv.* **2016**, *6*, No. 055105.
(59) Feng, W.; Luo, H.; Wang, Y.; Zeng, S.; Deng, L.; Zhou, X.; Zhang, H.; Peng, S. Ti_3C_2 MXene: a promising microwave absorbing material. *RSC Adv.* **2018**, *8*, 2398−2403.
(60) Balamurugan, B.; Maruyama, T. Evidence of an Enhanced Interband Absorption in Au Nanoparticles: Size-Dependent Electronic Structure and Optical Properties. *Appl. Phys. Lett.* **2005**, *87*, No. 143105.
(61) Lee, S. H.; Lee, K.-S.; Sorcar, S.; Razzaq, A.; Grimes, C. A.; In, S.-II Wastewater treatment and electricity generation from a sunlight-powered single chamber microbial fuel cell. *J. Photochem. Photobiol., A* **2018**, *358*, 432−440.

DOI: 10.1021/acsomega.8b01951
ACS Omega 2018, 3, 13828−13836